scientific reports

Check for updates

OPEN

Work extraction from coupled qubits in equilibrium and nonequilibrium thermal reservoirs

Maryam Hadipour[1] & Soroush Haseli[1,2]✉

This study investigates the thermodynamic behavior of a two-qubit quantum system, where each qubit is coupled to an independent thermal reservoir, either bosonic or fermionic. Using a master equation approach, we analyze both steady-state and time-dependent ergotropy to understand how different reservoir statistics affect work extraction. In bosonic environments, ergotropy consistently declines with increasing temperature due to thermal noise. In contrast, fermionic reservoirs exhibit more complex behavior, with ergotropy enhanced by particle transport under non-equilibrium conditions. Our results reveal a threshold-like sensitivity to the chemical potential configuration, leading to qualitatively distinct regimes of energy storage performance. Time-resolved analyses show that the system's approach to steady state varies depending on the type of reservoir and the coupling strength between qubits. These insights highlight how carefully engineered reservoir properties and non-equilibrium driving can be leveraged to optimize quantum battery performance.

Keywords Ergotropy, Non-equilibrium, Quantum coherence

Historically, thermodynamics has been associated with systems composed of a vast number of particles. Thermodynamics is a fundamental component of our current understanding of the physical world. It has stayed the same even through major revolutions in physics, such as relativity and quantum theory. Thermodynamics was initially introduced to study thermal systems on a macroscopic scale, before the advent of quantum mechanics at the microscopic level. However, with the advent of quantum mechanics, clear differences are observed in dealing with microscopic thermal systems compared to macroscopic systems. In the quantum regime, the behavior of systems is governed by quantum mechanics, where the principles of superposition, entanglement, and quantization come into play[1–7]. The laws of traditional thermodynamics, when applied within the realm of quantum mechanics, have led to the emergence of a new field in quantum theory known as quantum thermodynamics[8–13]. In quantum thermodynamics, efficient work extraction from quantum systems is a fundamental goal in studying quantum biological systems and modern nanoscale technologies. To determine the amount of extractable work from a quantum system, the concept of "ergotropy" is commonly used. Ergotropy refers to the maximum amount of work that can be extracted from a quantum system through employing cyclic unitary operations[14].

In practical scenarios, a quantum system unavoidably engages with its surrounding reservoirs. So, study of open quantum systems has attracted significant interest in quantum information theory[15]. The convergence of the concepts of open quantum systems and quantum thermodynamics has led to the expansion of operational quantum devices, such as quantum heat engines[16], quantum refrigerators[17], and quantum batteries[18–68]. It is thus critical to study work extraction in the context of open quantum systems. In recent years, there has been an increasing fascination with exploring open quantum systems in non-equilibrium settings[69–72]. The reservoirs remain out of equilibrium due to a steady temperature difference or chemical potential difference. This causes energy or matter flow through the quantum system and reservoirs, continuously keeping them away from thermodynamic equilibrium[73–76].

The simplest model imaginable for studying extractable work in non-equilibrium steady states is likely a two-qubit system coupled with two reservoirs[77,78]. In this work, we revisit such a system by analyzing the steady-state and dynamical ergotropy of two coupled qubits interacting with either bosonic or fermionic thermal reservoirs[79]. Our analysis reveals that bosonic and fermionic statistics induce fundamentally different behaviors in ergotropy under both equilibrium and non-equilibrium conditions. In bosonic reservoirs, ergotropy decreases monotonically with temperature, and is further suppressed by increased qubit coupling. In contrast, fermionic reservoirs exhibit a more intricate dependence: ergotropy increases with chemical potential bias $\Delta\mu$, showing

[1]Faculty of Physics, Urmia University of Technology, Urmia, Iran. [2]School of Quantum Physics and Matter, Institute for Research in Fundamental Sciences (IPM), P.O. 19395-5531, Tehran, Iran. ✉email: soroush.haseli@gmail.com

saturation behavior, and displays threshold-like sensitivity to the base chemical potential μ_1 in relation to the qubit transition frequency. The study also highlights that coherent dynamics and non-equilibrium driving—via temperature gradients or chemical potential differences—can dynamically generate ergotropy, even from initially passive states. Moreover, it shows that the extractable work from asymmetric qubits is highly sensitive to reservoir asymmetries, with maximum ergotropy achieved under symmetric conditions and equilibrium reservoirs.

Models and methods

The schematic diagram of the model is shown in Fig. 1. The model consists of two qubits that are coupled to each other, with each qubit interacting with its own reservoir. The reservoirs follow either fermionic or bosonic statistics. The total Hamiltonian of the system, which includes the coupled qubits and their respective reservoirs, can be written as $H = H_S + H_R + H_{\text{int}}$, where H_S, H_R, and H_{int} represent the system, reservoir, and interaction Hamiltonians, respectively. These components are defined as follows

$$\begin{aligned} H_s &= \omega_1 |e\rangle_1 \langle e| + \omega_2 |e\rangle_2 \langle e| + \frac{\lambda}{2}\left[\sigma_+^{(1)}\sigma_-^{(2)} + \sigma_-^{(1)}\sigma_+^{(2)}\right], \\ H_R &= \sum_k \omega_{1k} b_k^\dagger b_k + \sum_k \omega_{2k} c_k^\dagger c_k, \\ V &= \sum_k g_{1k}\left[\sigma_-^{(1)} b_k^\dagger + \sigma_+^{(1)} b_k\right] + \sum_k g_{2k}\left[\sigma_-^{(2)} c_k^\dagger + \sigma_+^{(2)} c_k\right] \end{aligned} \tag{1}$$

Here, ω_1 and ω_2 are the transition frequencies of the qubits, and λ denotes the coupling strength between the qubits. The operators b_k ($b_k^\dagger$) and c_k ($c_k^\dagger$) are the annihilation (creation) operators for the kth mode of the reservoirs, with mode frequencies ω_{1k} and ω_{2k}, which are in contact with qubits 1 and 2, respectively. The parameters g_{1k} and g_{2k} represent the coupling strengths between the reservoirs and qubits 1 and 2, respectively. The eigenvalues and the corresponding eigenvectors of the coupled qubit Hamiltonian are given by

$$\begin{aligned} \varepsilon_1 &= 0, \qquad |\varepsilon_1\rangle = |gg\rangle, \\ \varepsilon_2 &= \frac{\delta - \Omega}{2}, \qquad |\varepsilon_2\rangle = -\sin\frac{\theta}{2}|eg\rangle + \cos\frac{\theta}{2}|ge\rangle, \\ \varepsilon_3 &= \frac{\delta + \Omega}{2}, \qquad |\varepsilon_2\rangle = \cos\frac{\theta}{2}|eg\rangle - \sin\frac{\theta}{2}|ge\rangle, \\ \varepsilon_4 &= \delta, \qquad |\varepsilon_4\rangle = |ee\rangle, \end{aligned} \tag{2}$$

Here, $\delta = \omega_1 + \omega_2$, and $\Omega = \sqrt{\Delta^2 + \lambda^2}$ is the Rabi frequency, where $\Delta = \omega_1 - \omega_2$. The mixing angle $\theta \in [0, \pi]$ is defined as $\theta = \arctan(\lambda/\Delta)$.

In the case of symmetric qubits, i.e., when $\Delta = 0$, the mixing angle becomes $\theta = \pi/2$. For asymmetric qubits, i.e., $\omega_1 \neq \omega_2$, the mixing angle is given by $\theta = \arctan(\lambda/\Delta)$ when $\omega_1 > \omega_2$, and by $\theta = \pi + \arctan(\lambda/\Delta)$ when $\omega_1 < \omega_2$.

To ensure the validity of the rotating wave approximation in the qubit-reservoir interaction Hamiltonian, the condition $\lambda < 2\sqrt{\omega_1\omega_2}$ must be satisfied. This requirement ensures that $\delta > \Omega$, which allows the eigenenergies to be ordered as $\varepsilon_1 < \varepsilon_2 < \varepsilon_3 < \varepsilon_4$.

Figure 2 shows the schematic diagram of the eigenenergies and the corresponding eigenstates of the Hamiltonian for the coupled qubit system.

The unitary transformation between the energy eigenbasis $\{|\varepsilon_1\rangle, |\varepsilon_2\rangle, |\varepsilon_3\rangle, |\varepsilon_4\rangle\}$ and the standard eigenbasis $\{|ee\rangle, |eg\rangle, |ge\rangle, |gg\rangle\}$ is defined as follows

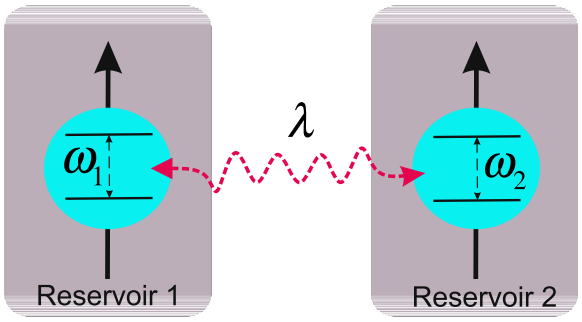

Fig. 1. The schematic diagram of the considered model includes two interacting qubits in two separate reservoirs. λ represents the inter-qubit coupling strength, and ω_1 and ω_2 are the energy level differences between the ground and excited states for the qubits.

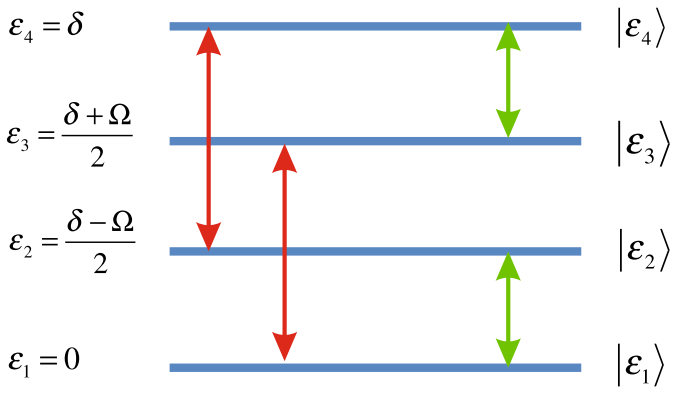

Fig. 2. The schematic diagram of eigenenergies ε_i and the corresponding eigenstates $|\varepsilon_i\rangle$ of the Hamiltonian for the coupled qubit system with $i = 1, 2, 3, 4$.

$$U = \begin{pmatrix} 1 & 0 & 0 & 0 \\ 0 & \cos\frac{\theta}{2} & \sin\frac{\theta}{2} & 0 \\ 0 & -\sin\frac{\theta}{2} & \cos\frac{\theta}{2} & 0 \\ 0 & 0 & 0 & 1 \end{pmatrix}. \tag{3}$$

The interaction term of the total Hamiltonian in energy eigenbasis can be rewritten as

$$H_{int} = \sum_k [g_{1k}(A_1 + B_1)b_k^\dagger + g_{2k}(A_2 + B_2)c_k^\dagger] + H.c., \tag{4}$$

where

$$\begin{aligned} A_1 &= \sin\frac{\theta}{2}(|\varepsilon_3\rangle\langle\varepsilon_4| - |\varepsilon_1\rangle\langle\varepsilon_2|), \\ B_1 &= \cos\frac{\theta}{2}(|\varepsilon_2\rangle\langle\varepsilon_4| + |\varepsilon_1\rangle\langle\varepsilon_3|), \\ A_2 &= \cos\frac{\theta}{2}(|\varepsilon_3\rangle\langle\varepsilon_4| + |\varepsilon_1\rangle\langle\varepsilon_2|), \\ B_2 &= \sin\frac{\theta}{2}(|\varepsilon_1\rangle\langle\varepsilon_3| - |\varepsilon_2\rangle\langle\varepsilon_4|). \end{aligned} \tag{5}$$

Considering free Hamiltonian $H_0 = H_S + H_R$ and using interaction picture we have

$$\begin{aligned} H_{int}(t) = &\sum_k g_{1k}\left(A_1 e^{-i\frac{\delta-\Omega}{2}t} + B_1 e^{-i\frac{\delta+\Omega}{2}t}\right) b_k^\dagger e^{i\omega_{1k}t} \\ &+ \sum_k g_{2k}\left(A_2 e^{-i\frac{\delta-\Omega}{2}t} + B_2 e^{-i\frac{\delta+\Omega}{2}t}\right) c_k^\dagger e^{i\omega_{2k}t} + H.c. \end{aligned} \tag{6}$$

In the interaction picture, the quantum master equation under the Born-Markov approximation is given by[15]

$$\frac{d\rho_I(t)}{dt} = -\int_0^\infty ds Tr_B\left[H_{int}(t), [H_{int}(t-s), \rho_I(t) \otimes (t)\rho_B]\right], \tag{7}$$

here, $\rho_I(t)$ and ρ_B denote the reduced density operator of the two-qubit system in the interaction picture, and the density operator of the reservoirs at equilibrium, respectively. At this stage, by returning to the Schrödinger picture and avoiding the secular approximation, one ultimately obtains the master equation known as the Bloch–Redfield equation for the system's density matrix

$$\frac{d\rho}{dt} = -i[H_S, \rho] + \mathscr{D}_1[\rho] + \mathscr{D}_2[\rho], \tag{8}$$

where $\mathscr{D}_1[\rho] = \sum_{j=1}^2 \mathscr{N}_j(\rho)$ and $\mathscr{D}_2[\rho] = \sum_{j=1}^2 \mathscr{S}_i(\rho)$ with

$$\begin{aligned}\mathscr{N}_i[\rho] =&\gamma_i^+ \left[2B_i^\dagger \rho B_i - B_i B_i^\dagger \rho - \rho B_i B_i^\dagger\right] \\ &+ \gamma_i^- \left[2A_i^\dagger \rho A_i - A_i A_i^\dagger \rho - \rho A_i A_i^\dagger\right] \\ &+ \Gamma_i^+ \left[2B_i \rho B_i^\dagger - B_i^\dagger B_i \rho - \rho B_i^\dagger B_i\right] \\ &+ \Gamma_i^- \left[2A_i \rho A_i^\dagger - A_i^\dagger A_i \rho - \rho A_i^\dagger A_i\right],\end{aligned} \tag{9}$$

and

$$\begin{aligned}\mathscr{S}_i[\rho] =&\gamma_i^+ \left[A_i^\dagger \rho B_i + B_i^\dagger \rho A_i - A_i B_i^\dagger \rho - \rho B_i A_i^\dagger\right] \\ &+ \gamma_i^- \left[A_i^\dagger \rho B_i + B_i^\dagger \rho A_i - B_i A_i^\dagger \rho - \rho A_i B_i^\dagger\right] \\ &+ \Gamma_i^+ \left[A_i \rho B_i^\dagger + B_i \rho A_i^\dagger - A_i^\dagger B_i \rho - \rho B_i^\dagger A_i\right] \\ &+ \Gamma_i^- \left[A_i \rho B_i^\dagger + B_i \rho A_i^\dagger - B_i^\dagger A_i \rho - \rho A_i^\dagger B_i\right]\end{aligned} \tag{10}$$

where $\gamma^\pm \equiv \gamma_i(\delta/2 \pm \Omega/2)$ and $\Gamma^\pm \equiv \Gamma_i(\delta/2 \pm \Omega/2)$. In boson reservoir we have

$$\gamma_i(\omega) = J_i(\omega)N_i(\omega), \quad \Gamma_i(\omega)[N_i(\omega)+1], \tag{11}$$

while for fermion reservoirs we have

$$\gamma_i(\omega) = J_i(\omega)N_i(\omega), \quad \Gamma_i(\omega)[1-N_i(\omega)]. \tag{12}$$

In the above equations, $J_i(\omega) = \pi \sum_k g_{ik}^2 \delta(\omega - \omega_{ik})$ is the spectral density of the ith reservoir [79]. The average particle number at a given frequency ω in the ith reservoir is described by $N_i(\omega) = \left(e^{\frac{\omega-\mu_i}{T_i}} \pm 1\right)^{-1}$, where the minus sign corresponds to bosonic reservoirs (following Bose–Einstein statistics) and the plus sign to fermionic reservoirs (following Fermi–Dirac statistics). Here, μ_i denotes the chemical potential, and T_i is the temperature of the ith reservoir.

In practical scenarios involving bosonic reservoirs, such as photon or phonon baths, the number of particles is generally not conserved, so the chemical potential becomes zero. This simplifies the expression for the bosonic case to $N_i(\omega) = \left(e^{\omega/T_i} - 1\right)^{-1}$. In contrast, fermionic reservoirs maintain a well-defined chemical potential, i.e., $\mu_i \neq 0$, allowing the system to exchange particles with the reservoir during the process.

At this stage, we assume balanced and frequency-independent spectral densities, such that $J_1(\delta/2 \pm \Omega/2) = J_2(\delta/2 \pm \Omega/2) = J$. To gain a clearer understanding of the physical processes described by the quantum master equation, we note that the structure of the interaction Hamiltonian $H_{\rm int}$ in Eq. (6) implies that the interaction between the two-qubit system and the reservoirs induces two distinct sets of energy-level transitions, as illustrated in Fig. 2.

One set includes the transitions $|\varepsilon_1\rangle \leftrightarrow |\varepsilon_2\rangle$ and $|\varepsilon_3\rangle \leftrightarrow |\varepsilon_4\rangle$, with transition frequency $(\delta - \Omega)/2$, shown as green arrows. The other set includes the transitions $|\varepsilon_2\rangle \leftrightarrow |\varepsilon_4\rangle$ and $|\varepsilon_1\rangle \leftrightarrow |\varepsilon_3\rangle$, with transition frequency $(\delta + \Omega)/2$, shown as red arrows. The dissipator term $\mathscr{D}_0[\rho]$ characterizes processes in which energy emitted to the reservoir from a transition is reabsorbed by another transition within the same frequency group. Meanwhile, the dissipator term $\mathscr{D}_1[\rho]$ describes processes involving emission and reabsorption between transitions belonging to different frequency groups.

The process associated with $\mathscr{D}_2[\rho]$ is typically regarded as a rapidly oscillating process and is eliminated using the secular approximation. The secular approximation works well at equilibrium situations. ($T_1 = T_2$) and ($\mu_1 = \mu_2, T_1 = T_2$) are the equilibrium situations for boson and fermion reservoirs respectively. Under these circumstances, the diagonal components of the density matrix become independent of the off-diagonal ones. The density matrix in the equilibrium steady state is diagonal, devoid of any remaining coherence in the energy eigenstate depiction. However, the non-equilibrium situation for boson reservoirs is $T_1 \neq T_2$ and for fermion reservoir is $\mu_1 \neq \mu_2$ and $T_1 \neq T_2$. Here, we aim to study the maximum extractable work from the dynamical system and steady state system under different reservoiral situations. Therefore, before anything else, we will briefly review the concept of ergotropy. Ergotropy is defined as the highest amount of energy that can be obtained from a quantum system via a cyclic unitary operation with unitary operation U[14]. So, the ergotropy can be given by $\mathscr{E}(\rho) = \mathscr{U}(\rho) - \min_U Tr(H_s U \rho U^\dagger)$, where $\mathscr{U}(\rho) = Tr(\rho H_s)$ is the internal energy of the system and H is the Hamiltonian of the considered system. In mentioned ergotropy formula the optimization is taken over the all set of the unitary operations U. It has been demonstrated that for any arbitrary state ρ, there is a unique state $\mathscr{P}_\rho$ that maximizes the given equation. The state $\mathscr{P}_\rho$ is called passive state. Hence, the ergotropy can be rewritten as $\mathscr{E}(\rho) = \mathscr{U}(\rho) - Tr(P_\rho H_s)$. Now, let's consider the spectral decomposition of the density matrix ρ and the system Hamiltonian H_s as follows

$$\begin{aligned}\rho &= \sum_n r_n |r_n\rangle\langle r_n|, \quad r_n \geq r_{n+1}, \\ H_s &= \sum_m \varepsilon_m |\varepsilon_m\rangle\langle\varepsilon_m|, \quad \varepsilon_m \leq \varepsilon_{m+1}.\end{aligned} \tag{13}$$

From above the passive state can be given by $\mathscr{P}_\rho = \sum_n r_n |\varepsilon_n\rangle\langle\varepsilon_n|$, where r_n ($|r_n\rangle$) and ε_m ($|\varepsilon_m\rangle$) are eigenvalues (eigenstates) of the density matrix ρ and Hamiltonian H_s respectively. So, the close form for ergotropy $\mathscr{E}(\rho)$ can be obtained as

$$\mathscr{E}(\rho) = \sum_{n,m} r_n \varepsilon_m \left(|\langle r_n|\varepsilon_m\rangle|^2 - \delta_{m,n} \right), \tag{14}$$

where $\delta_{m,n}$ is the Kronecker delta function.

Time-dependent ergotropy

Before addressing the steady-state thermodynamics of the system, we investigate the transient dynamics of *ergotropy*, which quantifies the amount of extractable work under unitary operations. Ergotropy serves as a powerful tool to assess how far a quantum system is from thermodynamic equilibrium and reveals non-passive features of quantum states that are not captured by internal energy alone. To explore these nonequilibrium aspects, we solve the full time-dependent master equation derived previously—without invoking the secular approximation—within the Schrödinger picture. The numerical simulations are carried out using the `QuTiP` library (Quantum Toolbox in Python), which provides a robust framework for modeling the dynamics of open quantum systems via the Bloch-Redfield formalism [80]. We assume that the initial state of the two-qubit system is the ground state, $\rho(0) = |g\rangle\langle g| \otimes |g\rangle\langle g|$, where both qubits are prepared in their respective lowest energy levels. Physically, this configuration corresponds to a fully passive state, from which no work can initially be extracted. As the system interacts with nonequilibrium fermionic or bosonic reservoirs, quantum coherences and populations are dynamically generated. The emergence of ergotropy during evolution thus reflects the ability of the reservoirs to temporarily drive the system into active, work-extractable states—even when starting from a thermodynamically inert configuration. This highlights how quantum reservoirs and coherence can play a crucial role in dynamical work resources, offering insights into quantum thermodynamic cycles beyond steady-state analysis.

Time-dependent ergotropy in the presence of equilibrium and non-equilibrium bosonic reservoirs

To elucidate the influence of the environmental configuration on work extraction in our quantum system, Here, we investigate the dynamics of ergotropy under both equilibrium and non-equilibrium bosonic reservoirs. In the *equilibrium* case, both qubits are locally coupled to identical bosonic thermal reservoirs at temperature T and with vanishing chemical potential. The dissipative interactions are governed by Bose-Einstein statistics, with the occupation number given by $N(\omega) = 1/(e^{\omega/T} - 1)$. Although the reservoirs are thermodynamically balanced and no net energy flow is expected at the steady state, transient ergotropy can still emerge during the evolution due to the interplay of quantum coherence and non-secular effects. This is especially relevant when the inter-qubit coupling λ is finite, enabling coherent energy exchange and population mixing. Even starting from a passive initial state, such as the joint ground state $\rho(0) = |g\rangle\langle g| \otimes |g\rangle\langle g|$, the system temporarily departs from thermodynamic equilibrium, exhibiting non-zero ergotropy. This reveals that equilibrium environments are capable of activating work resources dynamically, without requiring temperature gradients.In contrast, for the *non-equilibrium* configuration, the two qubits are coupled to separate bosonic reservoirs held at distinct temperatures $T_1 \neq T_2$. This thermal imbalance leads to directional energy flow across the system and breaks detailed balance. As a result, both the populations and coherences evolve asymmetrically, and the system is driven further away from equilibrium.

To illustrate the impact of temperature and temperature gradients on work extraction, we present in Fig. 3 the time evolution of the ergotropy $\mathscr{E}(\rho)$ for a two-qubit system coupled to bosonic reservoirs. In Fig. 3a, we consider the case of equilibrium reservoirs where both qubits are coupled to baths at the same temperature T, and explore several values ranging from $T = 0.2$ to $T = 0.8$. As can be seen, ergotropy initially rises from zero, reflecting the fact that the system begins in its ground state, and then saturates to a steady value. Notably, lower reservoir temperatures support the work extraction, which is attributed to the suppression of thermal noise and the enhanced preservation of quantum coherence. In equilibrium bosonic reservoirs, increasing the temperature enhances the rate of both absorption and emission processes, driving the system rapidly toward a thermal (passive) state. Since ergotropy quantifies the extractable work from non-passive states, thermalization at higher temperatures reduces population inversion and coherence, thereby diminishing the system's ergotropy. In contrast, panel (b) depicts the nonequilibrium case, where the two qubits are each coupled to bosonic reservoirs with different temperatures T_1 and T_2, creating a finite temperature bias $\Delta T = T_2 - T_1$. Here, T_1 is held fixed while ΔT is varied from 0 (equilibrium) to 2.0. The results clearly show that the presence of a thermal gradient boosts the transient and long-time values of the ergotropy. Even for moderate values of ΔT, the system is driven further from equilibrium, enabling the development of coherence and population imbalances that are inaccessible under thermal symmetry. This demonstrates that nonequilibrium bosonic environments can act as dynamical work resources, generating ergotropy even when starting from a fully passive initial configuration. Together, these two configurations highlight how both coherent system dynamics and reservoir engineering—via temperature control—play vital roles in regulating ergotropy. They further demonstrate that ergotropy is a sensitive probe of non-equilibrium behavior, capable of revealing transient quantum thermodynamic resources even in the absence of classical driving or steady-state currents.

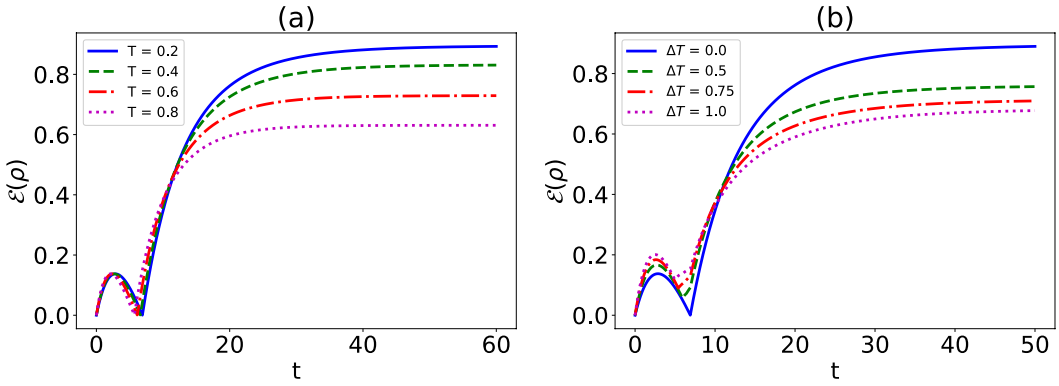

Fig. 3. (**a**) Time evolution of ergotropy $\mathscr{E}(\rho)$ for a two-qubit system coupled to an equilibrium bosonic reservoir at different temperatures $T = 0.2, 0.4, 0.6, 0.8$. (**b**) Ergotropy dynamics for a system coupled to a non-equilibrium bosonic reservoir with fixed $T_1 = 0.2$ and varying temperature differences $\Delta T = T_2 - T_1 = 0.0, 0.5, 0.75, 1.0$. In both panels, the system parameters are $\omega_1 = \omega_2 = 1$, $J = 0.1$, and $\lambda = 0.2$.

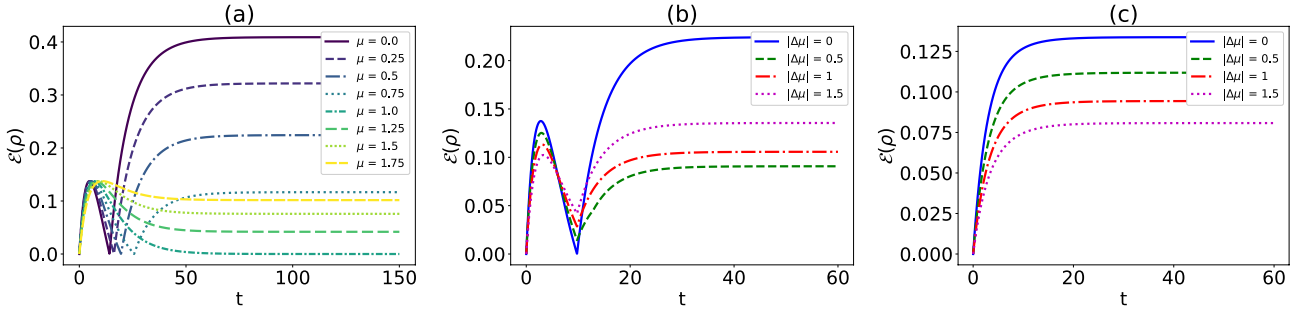

Fig. 4. Time evolution of ergotropy for a two-qubit system coupled to fermionic reservoirs. (**a**) Dynamics under equilibrium conditions for various values of the chemical potential μ. (**b**) Nonequilibrium dynamics for $\mu_1 = 0.5 < \omega$ and varying $\Delta\mu$. (**c**) Nonequilibrium dynamics for $\mu_1 = 3 > \omega$. The parameters are $T = 1.5$, $\lambda = 0.2$, $J = 0.1, \omega_1 = \omega_2 = 1$.

Time-dependent ergotropy in the presence of equilibrium and non-equilibrium fermionic reservoirs

We now consider the dynamics of ergotropy when the two-qubit system is coupled to fermionic reservoirs. In fermionic systems, particle exchange occurs according to the Fermi-Dirac distribution, which is strongly influenced by the chemical potential μ. This allows us to explore the role of electronic reservoirs in generating or suppressing ergotropy through both equilibrium and non-equilibrium configurations.

In the equilibrium case, both qubits are coupled to identical fermionic baths characterized by the same temperature and chemical potential. In contrast, under non-equilibrium conditions—where the chemical potentials of the two fermionic reservoirs are different and the system experiences asymmetric particle exchange. This chemical potential gradient drives the system away from equilibrium.

In Fig. 4a, the time-dependent dynamics of ergotropy are illustrated for various values of the chemical potential μ under equilibrium conditions, where both fermionic reservoirs are set to the same μ. The plot reveals complex and nontrivial behavior in the ergotropy evolution that varies significantly depending on the chemical potential. Specifically, two distinct dynamical regimes emerge, separated by the condition $\mu = \omega$. For $\mu < \omega$, the ergotropy initially increases rapidly, reaching a relative maximum, followed by a transient decrease toward zero. Interestingly, at this stage a sudden revival occurs, after which the ergotropy increases again and asymptotically approaches a steady-state value. Notably, within this regime, increasing the chemical potential leads to a decrease in the asymptotic value of the ergotropy, indicating suppression of work-extractable features. Conversely, in the regime $\mu > \omega$, the ergotropy also exhibits an initial growth and a subsequent peak; however, it then decreases smoothly and monotonically toward a steady value without any sudden revivals or fluctuations. Notably, within this regime, increasing the chemical potential leads to an increase in the asymptotic value of the ergotropy. This qualitative change in the dynamical pattern emphasizes the critical role of the chemical potential not only in determining the long-time value of the ergotropy, but also in shaping the transient behavior of the system.

This qualitative change in the ergotropy dynamics across the boundary $\mu = \omega$ arises from the way the chemical potential controls the population of energy eigenstates in fermionic reservoirs[79].

Figure 4b presents the time evolution of ergotropy for various values of the chemical potential difference $\Delta\mu$, with the baseline potential fixed at $\mu_1 = 0.5$. The results show that the maximum ergotropy is achieved under equilibrium conditions, where both fermionic reservoirs share the same chemical potential. Additionally, due to the condition $\mu_1 < \omega$, the dynamics exhibit sudden transitions, reflecting nontrivial transient behavior in the system's ability to store extractable work.

Figure 4c presents the time evolution of ergotropy for various values of the chemical potential difference $\Delta\mu$, with the baseline chemical potential set to $\mu_1 > \omega$. As shown, the maximum ergotropy is again attained under equilibrium conditions, where $\mu_1 = \mu_2$. In this high-μ regime, the dynamics exhibit smooth, monotonic behavior without sudden transitions. Notably, increasing the chemical potential difference $\Delta\mu$ results in a systematic reduction of the ergotropy, indicating that chemical imbalance suppresses the system's ability to generate and sustain extractable work over time.

Steady-state ergotropy

The steady state density matrix can be obtain by solving $d\rho/dt = 0$. Here, we just present the general form of the steady-state density matrix that results from the solution of $d\rho/dt = 0$. For more details on solving this equation, refer to Ref.[79]. In the absence of the secular approximation, the diagonal elements of the steady-state density matrix are coupled with the diagonal elements of the density matrix. Hence, the steady state density matrix in energy eigenstate ρ_ε can be obtained as

$$\rho_\varepsilon = \begin{pmatrix} \rho_{11} & 0 & 0 & 0 \\ 0 & \rho_{22} & \rho_{23} & 0 \\ 0 & \rho_{32} & \rho_{33} & 0 \\ 0 & 0 & 0 & \rho_{44} \end{pmatrix}. \tag{15}$$

Using Eq. (3), the steady state density matrix in general basis $\{|ee\rangle, |eg\rangle, |ge\rangle, |gg\rangle\}$ can be obtained as

$$\rho = \begin{pmatrix} \eta_{11} & 0 & 0 & 0 \\ 0 & \eta_{22} & \eta_{23} & 0 \\ 0 & \eta_{32} & \eta_{33} & 0 \\ 0 & 0 & 0 & \eta_{44} \end{pmatrix}. \tag{16}$$

where the element of the density matrix ρ are

$$\begin{aligned} \eta_{11} =& \rho_{11}, \quad \eta_{44} = \rho_{44}, \\ \eta_{22} =& \frac{1}{2}\left((\rho_{23} + \rho_{32})\sin\theta + \rho_{22}(\cos\theta + 1) - \rho_{33}(\cos\theta - 1)\right), \\ \eta_{33} =& \frac{1}{2}\left(\rho_{33}(\cos\theta + 1) - (\rho_{23} + \rho_{32})\sin\theta - \rho_{22}(\cos\theta + 1)\right), \\ \eta_{23} =& \frac{1}{2}\left((\rho_{33} - \rho_{22})\sin\theta + \rho_{23}(\cos\theta + 1) + \rho_{32}(\cos\theta - 1)\right), \end{aligned} \tag{17}$$

Equilibrium bosonic and fermionic reservoir

In equilibrium, both reservoirs have the same temperature and chemical potential i.e. $T_1 = T_2$ and $\mu_1 = \mu_2$. Here, the symmetric case is considered for the coupled qubits pair. So, we have $\omega_1 = \omega_2 = \omega$ and the mixing angle θ is equal to $\pi/2$. In this section, we aim to enhance the physical understanding of work extraction in equilibrium settings, areas that have been less explored in previous researches. At the the equilibrium steady state the off-diagonal element of density matrix will be vanished. The diagonal element can be obtained as[81]

$$\begin{aligned} \rho_{11} =& \frac{(\Gamma_1^+ + \Gamma_2^+)(\gamma_1^- + \gamma_2^-)}{\mathscr{Z}}, \\ \rho_{22} =& \frac{(\gamma_1^- + \gamma_2^-)(\gamma_1^+ + \gamma_2^+)}{\mathscr{Z}}, \\ \rho_{33} =& \frac{(\Gamma_1^- + \Gamma_2^-)(\gamma_1^+ + \gamma_2^+)}{\mathscr{Z}}, \\ \rho_{44} =& \frac{(\Gamma_1^- + \Gamma_2^-)(\Gamma_1^+ + \Gamma_2^+)}{\mathscr{Z}}, \end{aligned} \tag{18}$$

where $\mathscr{Z}$ is normalization factor which can be written as

$$\mathscr{Z} = (\gamma_1^- + \gamma_2^- + \Gamma_1^- + \Gamma_2^-)(\gamma_1^+ + \gamma_2^+ + \Gamma_1^+ + \Gamma_2^+). \tag{19}$$

To evaluate the steady-state properties of the system, it is essential to specify the explicit forms of the transition rates $\gamma_{1,2}^{\pm}$ and $\Gamma_{1,2}^{\pm}$, which characterize the excitation and relaxation processes induced by the reservoirs. These rates depend on the nature of the environment (bosonic or fermionic) as well as the reservoir temperature T and chemical potential μ. Using Eq. 11, the transition rates for the system interacting with equilibrium bosonic reservoirs (with equal temperatures $T_1 = T_2 = T$) are given by the following expressions:

$$\begin{aligned}\gamma_1^+ =&\gamma_2^+ = \frac{J}{e^{\omega_+/T}-1}, \quad \Gamma_1^+ = \Gamma_2^+ = \frac{Je^{\omega_+/T}}{e^{\omega_+/T}-1},\\ \gamma_1^- =&\gamma_2^- = \frac{J}{e^{\omega_-/T}-1}, \quad \Gamma_1^- = \Gamma_2^- = \frac{Je^{\omega_-/T}}{e^{\omega_-/T}-1},\end{aligned} \tag{20}$$

Here, J represents the system-reservoir coupling strength, and the dressed transition frequencies are defined as $\omega_\pm = \omega \pm \lambda/2$, where λ is the interqubit coupling strength. These rates reflect the bosonic nature of the environment, governed by the Bose-Einstein distribution. Due to the detrimental effects of thermal noise in equilibrium bosonic reservoirs on the maximum extractable work from coupled qubits, we now turn to fermionic reservoirs where particle exchange plays a crucial role. Specifically, we consider an equilibrium setup where the two fermionic reservoirs share the same temperature and chemical potential, i.e., $T_1 = T_2 = T$ and $\mu_1 = \mu_2 = \mu$.

In analogy with the bosonic case, and using Eq. (12), the transition rates are given by:

$$\begin{aligned}\gamma_1^+ =&\gamma_2^+ = \frac{J}{e^{\omega_{f+}/T}+1}, \quad \Gamma_1^+ = \Gamma_2^+ = \frac{Je^{\omega_{f+}/T}}{e^{\omega_{f+}/T}+1},\\ \gamma_1^- =&\gamma_2^- = \frac{J}{e^{\omega_{f-}/T}+1}, \quad \Gamma_1^- = \Gamma_2^- = \frac{Je^{\omega_{f-}/T}}{e^{\omega_{f-}/T}+1},\end{aligned} \tag{21}$$

where the fermionic transition frequencies are defined as

$$\omega_{f\pm} = \omega - \mu \pm \frac{\lambda}{2},$$

with ω the bare qubit transition frequency and λ the interqubit coupling strength. These rates reflect the Fermi-Dirac statistical nature of the reservoirs, and their dependence on the chemical potential μ allows for tunable energy exchange dynamics.

Non-equilibrium bosonic and fermionic resevoirs

In the previous section, we derived and analyzed the steady-state density matrix for both equilibrium bosonic and fermionic reservoirs, where the reservoirs shared identical temperatures and chemical potentials. Under such equilibrium conditions, the system approaches a thermal-like steady state, characterized by vanishing off-diagonal coherences in the energy eigenbasis.

We now turn to the non-equilibrium regime, where the reservoirs possess different thermodynamic properties. This includes scenarios where the bosonic reservoirs have unequal temperatures ($T_1 \neq T_2$) or where fermionic reservoirs are distinguished by different chemical potentials ($\mu_1 \neq \mu_2$). Such non-equilibrium settings induce persistent energy or particle currents through the system and lead to steady states that deviate from thermal equilibrium. Importantly, these nonequilibrium steady states may preserve quantum coherence and population imbalances, enabling the extraction of useful work. In what follows, we present the analytical structure of the steady-state density matrix for non-equilibrium bosonic and fermionic reservoirs, following the formalism introduced in Ref. [79].

We consider the symmetric configuration for the coupled qubits with $\omega_1 = \omega_2 = \omega$, implying a mixing angle $\theta = \pi/2$, detuning $\delta = 2\omega$, and effective coupling $\Omega = \lambda$. According to Ref. [79], the nonequilibrium density matrix can be written using the following notation:

$$\begin{aligned}L_+ =&\frac{1}{2}(N_1^+ + N_2^+), \quad L_- = \frac{1}{2}(N_1^- + N_2^-),\\ M_+ =&\frac{1}{2}(N_1^+ - N_2^+), \quad M_- = \frac{1}{2}(N_1^- - N_2^-),\end{aligned} \tag{22}$$

where $N_i^\pm = N_i(\delta/2 \pm \Omega/2)$ and $N_i(\omega)$ denotes the average particle number in the i-th reservoir at frequency ω. In this representation, $M_\pm$ encapsulate the non-equilibrium nature of the reservoirs: they vanish under equilibrium conditions and become nonzero otherwise. In contrast, $L_\pm$ represent the mean particle occupation and reflect the average equilibrium influence of the reservoirs.

Now, we focus on the case where the coupled qubits are embedded in individual bosonic reservoirs at different temperatures, i.e., $T_1 \neq T_2$, giving rise to a temperature gradient $\Delta T = T_2 - T_1$. The elements of the steady-state density matrix in the energy eigenbasis can be written as:

$$\begin{aligned}
\rho_{11} =& \frac{1}{\mathscr{N}}\left[(1+L_+)(1+L_-) - s_1 s_2 R\right], \\
\rho_{22} =& \frac{1}{\mathscr{N}}\left[L_-(1+L_+) + s_2 z_1 R\right], \\
\rho_{33} =& \frac{1}{\mathscr{N}}\left[L_+(1+L_-) + s_1 z_2 R\right], \\
\rho_{44} =& \frac{1}{\mathscr{N}}\left[L_+ L_- - z_1 z_2 R\right], \\
\rho_{23} =& \frac{1}{\mathscr{N}}\left[\frac{M_+(1+2L_-) + M_-(1+2L_+)}{2(1+L_+ + L_-) + i\frac{\Omega}{J}}\right],
\end{aligned} \tag{23}$$

where the auxiliary functions are defined as:

$$\begin{aligned}
s_1 =& M_+ - M_-(3 + 2L_+ + 2L_-), \\
s_2 =& M_- - M_+(3 + 2L_+ + 2L_-), \\
z_1 =& M_+ + M_-(1 + 2L_+ + 2L_-), \\
z_2 =& M_- + M_+(1 + 2L_+ + 2L_-), \\
R =& \frac{1}{4(1+L_+ + L_-)^2 + \left(\frac{\Omega}{J}\right)^2}.
\end{aligned} \tag{24}$$

The normalization factor $\mathscr{N}$ ensuring $\mathrm{Tr}(\rho) = 1$ is given by:

$$\begin{aligned}
\mathscr{N} =& (1+2L_+)(1+2L_-) \\
& -16 M_+ M_- (1+L_+ + L_-)^2 R.
\end{aligned} \tag{25}$$

Let us consider a system of coupled qubits, where each qubit is individually embedded in a Fermionic reservoir. In this configuration, both reservoirs are maintained at the same temperature, $T_1 = T_2$, while having different chemical potentials, $\mu_1 \neq \mu_2$. Consequently, a chemical potential difference $\Delta\mu = \mu_2 - \mu_1$ exists between the reservoirs.

In this non-equilibrium setting, the elements of the steady-state density matrix can be obtained analytically, as shown in Ref. [79]. The expressions for the population and coherence terms in the energy eigenbasis are given by:

$$\begin{aligned}
\rho_{11} =& (1-L_+)(1-L_-) - \mathscr{R}, \\
\rho_{22} =& L_-(1-L_+) + \mathscr{R}, \\
\rho_{33} =& L_+(1-L_-) + \mathscr{R}, \\
\rho_{44} =& L_+ L_- - \mathscr{R}, \\
\rho_{23} =& -\frac{M_+ + M_-}{2 + i\frac{\Omega}{J}},
\end{aligned} \tag{26}$$

where the non-equilibrium correction term $\mathscr{R}$ is defined as

$$\mathscr{R} = \frac{(M_+ + M_-)^2}{4 + \left(\frac{\Omega}{J}\right)^2}. \tag{27}$$

Steady-state ergotropy in equilibrium and non-equilibrium bosonic reservoirs

In this section, we study the steady-state work extraction in a scenario where the coupled qubits are influenced by bosonic equilibrium reservoirs with identical temperatures $T_1 = T_2$.

Figure 5a shows the steady-state ergotropy of the two-qubit system as a function of the reservoir temperature in the case of an equilibrium bosonic environment. The results reveal that ergotropy decreases monotonically with increasing temperature, indicating that thermal fluctuations reduce the amount of extractable work from the system. Additionally, the effect of interqubit coupling strength λ is illustrated, showing that stronger coupling leads to lower steady-state ergotropy. This suggests that stronger interaction between the qubits suppresses the coherence and population imbalance required for maintaining work-extractable states. Figure 5b further supports these findings by depicting the steady-state ergotropy as a function of temperature bias ΔT in the non-equilibrium case. Similar qualitative trends are observed, with ergotropy decreasing both with increasing ΔT and with increasing λ, confirming the detrimental effect of thermal and interaction-induced noise on the energetic performance of the system.

The results in Fig. 5 reveal that both thermal effects and interqubit coupling reduce the steady state work extraction from coupled qubit system in both equilibrium and non-equilibrium reservoirs. In the equilibrium bosonic case (Fig. 5a), increasing temperature leads to reduced ergotropy due to enhanced thermal fluctuations, which suppress coherence and population imbalance. Similarly, stronger interqubit coupling λ decreases ergotropy by mixing energy levels and disrupting optimal work-extractable states. In the non-equilibrium case

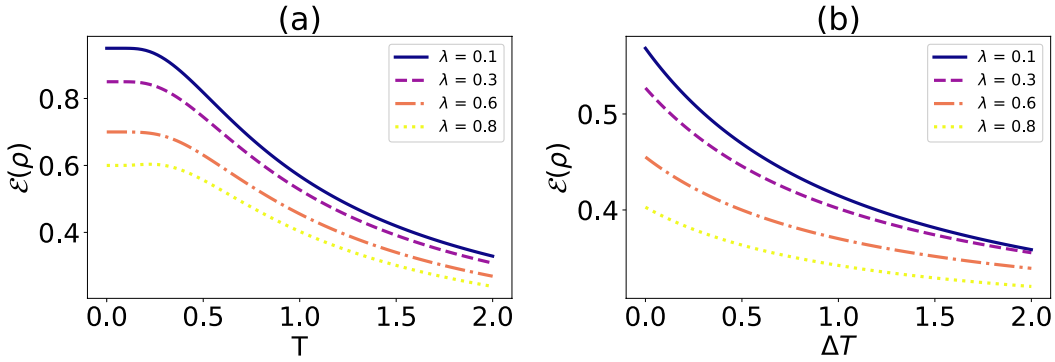

Fig. 5. (**a**) Time evolution of ergotropy $\mathscr{E}(\rho)$ for a two-qubit system coupled to an equilibrium bosonic reservoir at different temperatures $T = 0.2, 0.4, 0.6, 0.8$. (**b**) Ergotropy dynamics for a system coupled to a non-equilibrium bosonic reservoir with fixed $T_1 = 0.2$ and varying temperature differences $\Delta T = T_2 - T_1 = 0.0, 0.5, 0.75, 1.0$. In both panels, the system parameters are $\omega_1 = \omega_2 = 1$, $J = 0.1$, and $\lambda = 0.2$.

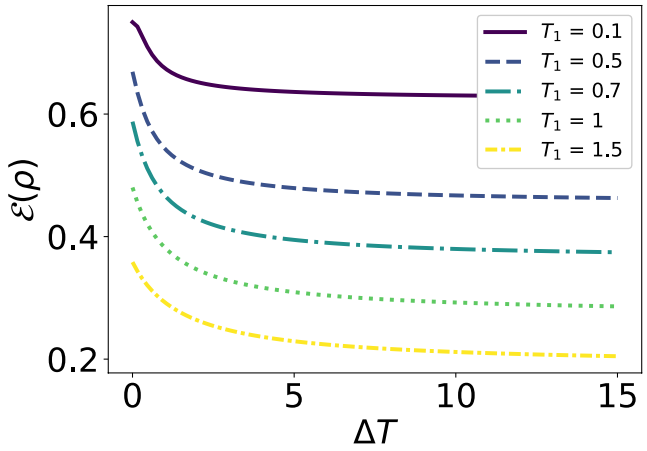

Fig. 6. Steady-state ergotropy as a function of temperature bias $\Delta T = T_2 - T_1$ for various values of T_1. The other parameters are fixed as $\omega_1 = \omega_2 = 1$, $\lambda = 0.5$, and $J = 0.1$.

(Fig. 5b), increasing the temperature bias ΔT also diminishes ergotropy, indicating that thermal noise—whether symmetric or asymmetric—has a detrimental effect on the energetic performance of the system. Figure 6 presents the steady-state ergotropy $\mathscr{E}(\rho)$ as a function of the temperature bias $\Delta T = T_2 - T_1$ for several fixed values of the base temperature T_1. As shown in the plot, the ergotropy decreases monotonically with increasing ΔT for all values of T_1. This behavior indicates that the presence of a thermal gradient—although it drives the system out of equilibrium—does not necessarily enhance the system's ability to store extractable work in the steady state. Physically, this decline can be attributed to the detrimental effects of thermal noise introduced by the hotter reservoir (with temperature $T_2 = T_1 + \Delta T$). As ΔT increases, the second reservoir becomes significantly hotter, promoting random thermal excitations and decoherence, which wash out quantum coherences and population imbalances—key ingredients for non-passive, work-extractable states. Additionally, the plot reveals that for a fixed ΔT, the steady-state ergotropy is higher when T_1 is lower. This implies that the colder the base reservoir, the more favorable the thermodynamic conditions are for maintaining coherence and population inversion within the two-qubit system. In contrast, increasing T_1 shifts the overall thermal environment to a higher average temperature, where thermal excitations from both reservoirs jointly suppress ergotropy. Overall, these results emphasize the importance of reservoir temperature management in quantum thermodynamic devices. While non-equilibrium conditions are necessary for energy transport, excessively high temperature gradients or average temperatures can degrade the energetic performance of the system. This highlights a subtle trade-off in engineering quantum batteries or heat engines: driving the system far from equilibrium must be balanced against the detrimental effects of thermal noise.

Fig. 7 shows the steady-state ergotropy of a two-qubit system coupled to fermionic reservoirs under various conditions. Figure 7a displays the ergotropy $\mathscr{E}(\rho)$ as a function of the chemical potential μ when both reservoirs are in equilibrium with the same chemical potential. The ergotropy initially increases with μ, reaches a maximum, and then gradually decreases as μ becomes large. This behavior indicates the existence of an optimal chemical potential at which the imbalance and coherence between the qubits are maximized, leading to

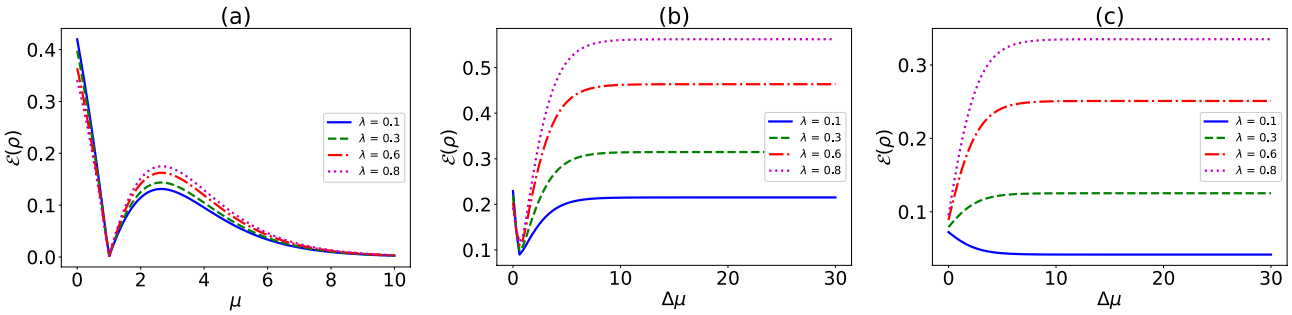

Fig. 7. (**a**) Steady-state ergotropy $\mathscr{E}(\rho)$ as a function of chemical potential μ for different values of the coupling strength λ, with temperature $T = 1.5$. (**b**) Ergotropy as a function of chemical potential difference $\Delta\mu = \mu_2 - \mu_1$ for various λ, with fixed $T = 1.5$ and $\mu_1 = 0.5$. (**c**) Same as (**b**), but with $\mu_1 = 1.5$. In all panels, the other parameters are $J = 0.1, \omega_1 = \omega_2 = 1$.

maximum extractable work. For higher values of the coupling strength λ, the peak occurs at a lower μ and with slightly higher ergotropy, reflecting the role of stronger qubit-qubit interaction in facilitating energy exchange and coherence buildup.

Figure 7b shows the ergotropy as a function of chemical potential difference $\Delta\mu = \mu_2 - \mu_1$, for a fixed $\mu_1 = 0.5$, representing a non-equilibrium scenario. In this regime, the chemical potentials lie below the system's transition frequencies ($\mu < \omega = 1$), placing the reservoirs in a low-occupation regime. As $\Delta\mu$ increases, the ergotropy increases and eventually saturates, indicating that larger chemical potential gradients provide greater energetic imbalance that can be harvested as useful work. The behavior in this low-μ regime is qualitatively distinct from that near or above $\mu = \omega$, where reservoir-induced excitations dominate. In the present case, the ergotropy builds up primarily due to the imbalance and coherence driven by the chemical potential difference, rather than by direct excitation. Notably, stronger interqubit coupling λ enhances the maximum achievable ergotropy, underscoring its critical role in mediating energy exchange and coherence, and thus in amplifying the system's capacity to extract work from non-equilibrium chemical resources. Here, the sudden change of ergotropy can be seen.

Figure 7c presents a similar plot to panel (b), but with a higher initial chemical potential $\mu_1 = 1.5$. In this case, the ergotropy at $\Delta\mu = 0$ is already non-zero and higher than in Fig.7b, due to increased occupation of fermionic modes. However, the saturation value of the ergotropy for large $\Delta\mu$ is slightly lower, suggesting that starting from a more populated state reduces the relative gain from increasing $\Delta\mu$. This reflects a trade-off: while higher μ_1 leads to higher initial ergotropy, it limits the capacity for further enhancement via chemical bias. Additionally, no sharp transition is observed at the margin where μ_2 crosses the system frequency ω, indicating a smooth and continuous evolution of ergotropy across this point. This contrasts with possible threshold-like behaviors and highlights that the system responds gradually to the chemical potential gradient.

Overall, the results demonstrate that the ergotropy is significantly affected by both the chemical potential configuration of the reservoirs and the interqubit coupling strength. Increasing $\Delta\mu$ enables greater work extraction due to stronger non-equilibrium driving, while increasing λ boosts the system's ability to exploit this driving by generating coherence and facilitating energy redistribution between the qubits.

Figure 8 presents the steady-state ergotropy $\mathscr{E}(\rho)$ as a function of the chemical potential difference $\Delta\mu = \mu_2 - \mu_1$, for several fixed values of the base chemical potential μ_1, in the context of fermionic reservoirs. The system parameters are set as $\omega_1 = \omega_2 = 1$, $\lambda = 0.1$, $J = 0.1$, and $T = 0.15$. The results reveal two distinct dynamical regimes depending on whether μ_1 is smaller or larger than the qubit transition frequency ω. When $\mu_1 < \omega$ (e.g., $\mu_1 = 0.25$ and 0.5), the ergotropy exhibits a pronounced dip at intermediate $\Delta\mu$ values, leading to a non-monotonic behavior. This sudden change suggests strong sensitivity to chemical potential imbalances, likely due to resonance effects that significantly alter the population distribution and coherence in the system. On the other hand, for $\mu_1 > \omega$ (e.g., $\mu_1 = 1.5$, 2, and 2.5), the ergotropy shows a much smoother and more gradual increase with $\Delta\mu$, eventually reaching a nearly saturated value. In this high-μ regime, the fermionic modes are already substantially populated, so further increases in $\Delta\mu$ have a limited effect on the system's energetic configuration.

Overall, the figure highlights a crossover around $\mu_1 \approx \omega$ that separates two qualitatively different behaviors: a sharp, resonance-sensitive response for $\mu_1 < \omega$, and a smoother, saturation-like response for $\mu_1 > \omega$. This transition point is important for understanding how to optimize ergotropy generation in fermionic quantum thermal machines.

Extracting work from asymmetric qubits

So far, we have studied the maximum extractable work from the coupled symmetric qubits with $\omega_1 = \omega_2$ at both boson and fermion reservoirs, with equilibrium and non-equilibrium scenario. Now, we intend to investigate the maximum extractable work from the coupled asymmetric qubits $\omega_1 \neq \omega_2$ at both fermion and boson reservoirs. To understand more details about how to obtain the elements of the steady-state density matrix, see Ref.[79]. The elements of the density matrix are introduced using the following formulation

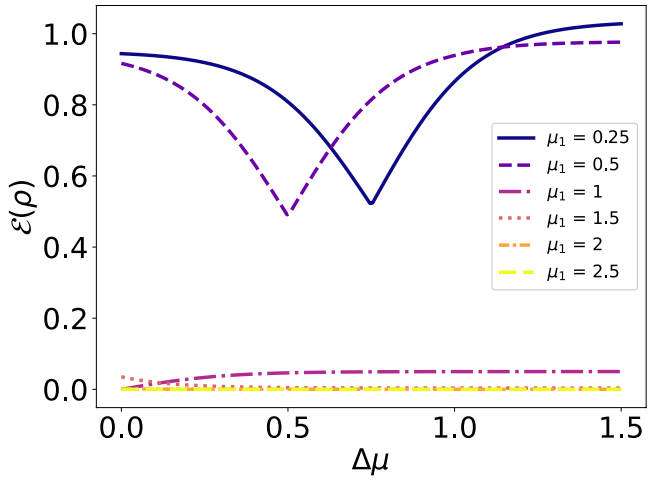

Fig. 8. Steady-state ergotropy as a function of the chemical potential bias $\Delta\mu = \mu_2 - \mu_1$ for various values of the initial chemical potential μ_1. The other parameters are fixed as $\omega_1 = \omega_2 = 1$, $\lambda = 0.1$, $J = 0.1$, and $T = 0.15$.

$$\mathscr{L}_\pm = L_\pm \pm M_\pm \cos\theta, \quad \mathscr{M}_\pm = M_\pm \sin\theta. \tag{28}$$

The elements of the density matrix in the antisymmetric situation will be obtained by substituting $\mathscr{L}_\pm$ and $\mathscr{M}_\pm$ instead of $L_\pm$ and $M_\pm$ in the symmetric case. So, the elements of the density matrix for asymmetric qubits coupled to boson reservoir are given by

$$\begin{aligned}
\rho_{11} =& \frac{1}{\mathscr{G}}\left[(1+\mathscr{L}_+)(1+\mathscr{L}_-) - s_1 s_2 R\right],\\
\rho_{22} =& \frac{1}{\mathscr{G}}\left[\mathscr{L}_-(1+\mathscr{L}_+) + s_2 z_1 R\right],\\
\rho_{33} =& \frac{1}{\mathscr{G}}\left[\mathscr{L}_+(1+\mathscr{L}_-) + s_1 z_2 R\right],\\
\rho_{44} =& \frac{1}{\mathscr{G}}\left[\mathscr{L}_+\mathscr{L}_- - z_1 z_2 R\right],\\
\rho_{23} =& \frac{1}{\mathscr{G}}\left[\frac{\mathscr{M}_+(1+2\mathscr{L}_-) + \mathscr{M}_-(1+2\mathscr{L}_+)}{2(1+\mathscr{L}_+ + \mathscr{L}_-) + i\frac{\Omega}{J}}\right],
\end{aligned} \tag{29}$$

with

$$\begin{aligned}
s_1 =& \mathscr{M}_+ - \mathscr{M}_-(3 + 2\mathscr{L}_+ + 2\mathscr{L}_-),\\
s_2 =& \mathscr{M}_- - \mathscr{M}_+(3 + 2\mathscr{L}_+ + 2\mathscr{L}_-),\\
z_1 =& \mathscr{M}_+ + \mathscr{M}_-(1 + 2\mathscr{L}_+ + 2\mathscr{L}_-),\\
z_2 =& \mathscr{M}_- + \mathscr{M}_+(1 + 2\mathscr{L}_+ + 2\mathscr{L}_-),\\
R =& \frac{1}{4(1+\mathscr{L}_+ + \mathscr{L}_-)^2 + (\frac{\Omega}{J})^2}.
\end{aligned} \tag{30}$$

where $\mathscr{G}$ is the normalization factor and is given by

$$\mathscr{G} = (1+2\mathscr{L}_+)(1+2\mathscr{L}_-) - 16\mathscr{M}_+\mathscr{M}_-(1+\mathscr{L}_+ + \mathscr{L}_-)^2 R. \tag{31}$$

Similarly, the elements of the density matrix for an asymmetric qubit coupled to the fermion reservoir will be obtained as follows

$$\begin{aligned}
\rho_{11} =& (1-\mathscr{L}_+)(1-\mathscr{L}_-) - \mathscr{R},\\
\rho_{22} =& \mathscr{L}_-(1-\mathscr{L}_+) + \mathscr{R},\\
\rho_{33} =& \mathscr{L}_+(1-L-) + \mathscr{R},\\
\rho_{44} =& L + \mathscr{L}_-\mathscr{R},\\
\rho_{23} =& -\frac{\mathscr{M}_+ + \mathscr{M}_-}{2 + i\frac{\Omega}{J}},
\end{aligned} \tag{32}$$

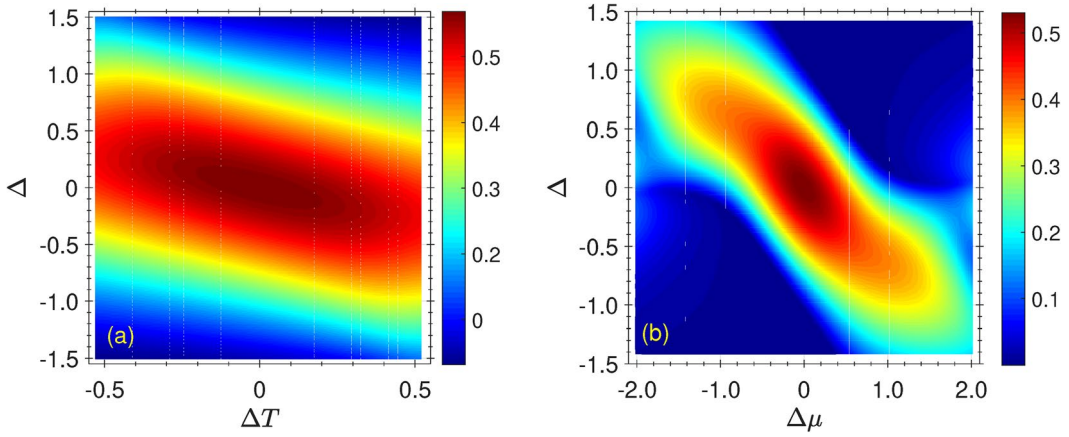

Fig. 9. (**a**) The steady-state ergotropy of coupled qubits embedded in boson reservoir as a function of temperature difference ΔT and detuning Δ with $\bar{T} = \frac{T_1+T_2}{2} = 0.3$. (**b**) The steady-state ergotropy of coupled qubits embedded in fermion reservoir as a function of chemical potential difference $\Delta\mu$ and detuning Δ with $\bar{\mu} = \frac{\mu_1+\mu_2}{2} = 0.4, T_1 = T_2 = 0.15$. The other parameters are set as $J_1 = J_2 = 0.1, \lambda = 0.6$ and $\bar{\omega} = \frac{\omega_1+\omega_2}{2} = 1$ for both panels.

where

$$\mathscr{R} = \frac{(\mathscr{M}_+ + \mathscr{M}_-)^2}{4 + (\frac{\Omega}{J})^2}. \tag{33}$$

Our results about the maximum work extraction of the asymmetric coupled qubits inside boson and fermion reservoirs have been shown in Fig. 9a and b, respectively. Figure 9, is the counter plot of the steady state maximum work extraction, decribed by ergotropy, as a function of the non-equilibrium parameter ΔT and $\Delta\mu$ for boson and fermion reservoirs, respectively and the detuning between transition frequency of the coupled qubits $\Delta = \omega_1 - \omega_2$ of the coupled qubits.

As shown in Fig. 9a, ergotropy is at its maximum value in the center of the phase diagram, i.e., under conditions where the boson reservoirs are in equilibrium situation and the qubits are symmetric. Therefore, it can be concluded that the maximum work will be extracted under conditions where the coupled qubits are symmetric and situated in the equilibrium reservoirs. It is also observed that the ergotropy has its minimum values at the top right and bottom left corners of the phase diagram. In the top right corner we have $\Delta > 0$ and $\Delta T > 0$ which are associated with $\omega_1 > \omega_2$ and $T_1 < T_2$, respectively, while in the bottom left corner $\omega_1 < \omega_2$ and $T_1 > T_2$. So, it can be concluded that putting the qubit with a higher transition frequency in a boson reservoir at a lower temperature does not lead to an optimal work extraction. From Fig. 9a, it can be seen the the ergotropy has its maximum value in the center of the phase diagram, i.e., under conditions where the fermion reservoirs are in equilibrium situation and the qubits are symmetric. Therefore, it can be concluded that the maximum work will be extracted under conditions where the coupled qubits are symmetric and situated in the equilibrium fermion reservoirs. It is also observed that the ergotropy has its minimum values at the top right and bottom left corners of the phase diagram. In the top right corner we have $\Delta > 0$ and $\Delta\mu > 0$ which are associated with $\omega_1 > \omega_2$ and $\mu_1 < \mu_2$, respectively, while in the bottom left corner $\omega_1 < \omega_2$ and $\mu_1 > \mu_2$. So, it can be concluded that putting the qubit with a higher transition frequency in a fermion reservoir at a lower chemical potential does not lead to an optimal work extraction.

Summary and results

In this study, we have systematically explored the thermodynamic properties of a two-qubit quantum system in contact with thermal reservoirs, focusing on the behavior of ergotropy under both equilibrium and non-equilibrium conditions. Each qubit was coupled to a local reservoir, which could be either bosonic or fermionic in nature. By employing the Lindblad master equation framework, we analyzed the system steady-state and time-dependent dynamics, with particular emphasis on how temperature, chemical potential, and inter-qubit coupling influence the amount of extractable work.

For bosonic reservoirs, our results reveal that the steady-state ergotropy decreases monotonically with increasing temperature. This is physically intuitive, as thermal fluctuations in a bosonic bath tend to drive the system toward a passive, high-entropy state where population differences and coherences—key ingredients for ergotropy—are suppressed. Additionally, we observed that increasing the inter-qubit coupling strength λ further reduces the steady-state ergotropy, indicating that stronger coupling inhibits the generation of useful energetic imbalance in the presence of bosonic noise. These results suggest that in bosonic environments, both thermal noise and interaction-induced decoherence play destructive roles in the work extraction process.

In stark contrast, fermionic reservoirs exhibit more intricate and nontrivial behavior. In the equilibrium scenario (equal temperature and chemical potential), the ergotropy displays a threshold-like dependence on

the base chemical potential μ. When $\mu < \omega$, the ergotropy remains low and increases slowly with μ. However, once μ exceeds the qubit transition frequency ω, the system becomes significantly populated due to Fermi-Dirac statistics, and the ergotropy rises sharply before eventually saturating. This threshold behavior highlights the importance of aligning chemical potential with the system's energy levels to optimize energy storage and retrieval.

In the non-equilibrium fermionic case, where a chemical potential difference $\Delta\mu = \mu_2 - \mu_1$ is introduced, we observed that ergotropy can be significantly enhanced through particle transport. However, the nature of this enhancement depends crucially on the base value of μ_1. For $\mu_1 < \omega$, the ergotropy exhibits a non-monotonic dependence on $\Delta\mu$, characterized by a sharp dip and then recovery—indicating a sensitive interplay between resonant energy exchange and the redistribution of populations across energy levels. For $\mu_1 > \omega$, this behavior becomes smooth and monotonic, with ergotropy gradually increasing and eventually saturating. This transition from sharp to smooth behavior around $\mu_1 \approx \omega$ suggests the existence of a resonance-like crossover regime that governs the efficiency of work extraction.

Moreover, unlike the bosonic case, increasing the inter-qubit coupling λ in fermionic reservoirs tends to enhance the ergotropy. This counterintuitive result can be attributed to the role of coherent energy exchange in the fermionic setting, where strong coupling helps maintain energetic asymmetries and coherences that contribute positively to the ergotropy.

Our time-dependent analysis further supports these observations. We demonstrate how the ergotropy evolves dynamically, approaching its steady-state value over time. The rate and nature of this convergence vary between bosonic and fermionic reservoirs, and are modulated by λ. In bosonic environments, the system relaxes toward a passive state, whereas in fermionic baths, persistent population imbalances allow for nontrivial ergotropy dynamics and richer energetic features.

In summary, this work provides a comprehensive understanding of the role of reservoir statistics in the thermodynamic performance of quantum batteries. It shows that by carefully tuning the temperature, chemical potential, and interaction strength, one can manipulate the ergotropy landscape and thereby optimize work extraction. Our results offer valuable guidelines for the practical implementation of quantum batteries, particularly in scenarios where fermionic reservoirs or non-equilibrium particle transport mechanisms are available. These insights may pave the way for designing next-generation energy-harvesting quantum devices that exploit statistical properties of their environments for maximal efficiency.

Data availability

Data sets generated during the current study are available from the corresponding author on reasonable request.

Received: 11 May 2025; Accepted: 25 August 2025
Published online: 28 August 2025

References

1. Horodecki, M. & Oppenheim, J. (Quantumness in the context of) Resource theories. *Int. J. Mod. Phys. B* **27**, 1345019 (2013).
2. Bennett, C. H., Bernstein, H., Popescu, S. & Schumacher, B. Concentrating partial entanglement by local operations. *Phys. Rev. A* **53**, 2046–2052 (1996).
3. Horodecki, R., Horodecki, P., Horodecki, M. & Horodecki, K. Quantum entanglement. *Rev. Mod. Phys.* **81**, 865–942 (2009).
4. Bartlett, S. D., Rudolph, T. & Spekkens, R. W. Reference frames, superselection rules, and quantum information. *Rev. Mod. Phys.* **79**, 555–609 (2007).
5. Horodecki, M., Horodecki, P. & Oppenheim, J. Reversible transformations from pure to mixed states and the unique measure of information. *Phys. Rev. A* **67**, 062104 (2003).
6. Marvian, I. & Spekkens, R. W. The theory of manipulations of pure state asymmetry: I. basic tools, equivalence classes and single copy transformations. *New J. Phys.* **15**, 033001 (2013).
7. Popescu, S., Short, A. J. & Winter, A. Entanglement and the foundations of statistical mechanics. *Nat. Phys.* **2**, 754–758 (2006).
8. Gemmer, J., Michel, M. & Mahler, G. *Quantum Thermodynamics: Emergence of Thermodynamic Behavior Within Composite Quantum Systems* Vol. 784 (Springer, 2009).
9. Kosloff, R. Quantum thermodynamics: A dynamical viewpoint. *Entropy* **15**, 2100 (2013).
10. Goold, J., Huber, M., Riera, A., del Rio, L. & Skrzypczyk, P. The role of quantum information in thermodynamics. *J. Phys. A: Math. Theor.* **49**, 143001 (2016).
11. Vinjanampathy, S. & Anders, J. Quantum thermodynamics. *Contemp. Phys.* **57**, 545 (2016).
12. Binder, F., Correa, L. A., Gogolin, C., Anders, J. & Adesso, G. Thermodynamics in the quantum regime fundamental aspects and new directions. *Fund. Theor. Phys.* **195**, 1 (2018).
13. Deffner, S. & Campbell, S. *Quantum Thermodynamics (An Introduction to the Thermodynamics of Quantum Information)* 2053–2571 (Morgan and Claypool Publishers, 2019).
14. Allahverdyan, A. E., Balian, R. & Nieuwenhuizen, Th. M. Maximal work extraction from quantum systems. *Europhys. Lett.* **67**, 565 (2004).
15. Breuer, H.-P. & Petruccione, F. *The Theory of Open Quantum Systems* (Oxford University Press/Cambridge University Press, 2007).
16. Bouton, Q. et al. *Nat. Commun.* **12**, 2063 (2021).
17. Maslennikov, G. et al. *Nat. Commun.* **10**, 202 (2019).
18. Joshi, J. & Mahesh, T. S. *Phys. Rev. A* **106**, 042601 (2022).
19. Zahia, A. A., Rabbou, M. Y. A. & Megahed, A. M. *J. Phys. B: At. Mol. Opt. Phys.* **58**, 065501 (2025).
20. Zhi-Guang, Lu., Tian, Guoqing, Xin-You, Lu. & Shang, Cheng. *Phys. Rev. Lett.* **134**, 180401 (2025).
21. Paolo Andrea Erdman. Gian Marcello Andolina, Vittorio Giovannetti, and Frank Noe. *Phys. Rev. Lett.* **133**, 243602 (2024).
22. Tabesh, F. T. & Kamin, F. H. S. Salimi. *Phys. Rev. A* **102**(5), 052223 (2020).
23. Kamin, F. H., Abuali, Z., Ness, H. & Salimi, S. *J. Phys. A: Math. Theor.* **56**(27), 275302 (2023).
24. Kamin, F. H. & Salimi, S. M. B. Arjmandi. *Phys. Rev. A* **109**(2), 022226 (2024).
25. Hadipour, M., Haseli, S., Wang, D. & Haddadi, S. arXiv preprint arXiv:2312.06389.
26. Hadipour, M., & Haseli, S. arXiv preprint arXiv:2303.17884.
27. Hadipour, M. & Haseli, S. arXiv preprint arXiv:2401.16111.
28. Zhu, G., Chen, Y., Hasegawa, Y. & Xue, P. *Phys. Rev. Lett.* **131**, 240401 (2023).

29. Andolina, G. M. et al. Charger-mediated energy transfer in exactly solvable models for quantum batteries. *Phys. Rev. B* **98**, 205423 (2018).
30. Le, T. P., Levinsen, J., Modi, K., Parish, M. M. & Pollock, F. A. Spin-chain model of a many-body quantum battery. *Phys. Rev. A* **97**, 022106 (2018).
31. Zhang, Y.-Y., Yang, T.-R., Fu, L. & Wang, X. Powerful harmonic charging in a quantum battery. *Phys. Rev. E* **99**, 052106 (2019).
32. Barra, F. Dissipative charging of a quantum battery. *Phys. Rev. Lett.* **122**, 210601 (2019).
33. Santos, A. C., Çakmak, B., Campbell, S. & Zinner, N. T. Stable adiabatic quantum batteries. *Phys. Rev. E* **100**, 032107 (2019).
34. Andolina, G. M. et al. Extractable work, the role of correlations, and asymptotic freedom in quantum batterie. *Phys. Rev. Lett.* **122**, 047702 (2019).
35. Crescente, A., Carrega, M., Sassetti, M. & Ferraro, D. Ultrafast charging in a two-photon Dicke quantum battery. *Phys. Rev. B* **102**, 245407 (2020).
36. Santos, A. C., Saguia, A. & Sarandy, M. S. Stable and charge-switchable quantum batteries. *Phys. Rev. E* **101**, 062114 (2020).
37. Santos, A. C. Quantum advantage of two-level batteries in the self-discharging process. *Phys. Rev. E* **103**, 042118 (2021).
38. Ghosh, S., Chanda, T., Mal, S. & De Sen, A. Fast charging of a quantum battery assisted by noise. *Phys. Rev. A* **104**, 032207 (2021) (**8**).
39. Delmonte, A., Crescente, A., Carrega, M., Ferraro, D. & Sassetti, M. Characterization of a two-photon quantum battery: Initial conditions, stability and work extraction. *Entropy* **23**, 612 (2021).
40. Li, J. L., Shen, H. Z. & Yi, X. X. Quantum batteries in non-Markovian reservoirs. *Opt. Lett.* **47**, 5614 (2022).
41. Dou, F.-Q., Lu, Y.-Q., Wang, Y.-J. & Sun, J.-A. Extended Dicke quantum battery with interatomic interactions and driving field. *Phys. Rev. B* **105**, 115405 (2022).
42. Barra, F., Hovhannisyan, K. V. & Imparato, A. Quantum batteries at the verge of a phase transition. *New J. Phys.* **24**, 015003 (2022).
43. Carrasco, J., Maze, J. R., Hermann-Avigliano, C. & Barra, F. Collective enhancement in dissipative quantum batteries. *Phys. Rev. E* **105**, 064119 (2022).
44. Shaghaghi, V., Singh, V., Benenti, G. & Rosa, D. Micromasers as quantum batteries. *Quantum Sci. Technol* **7**, 04LT01 (2022).
45. Rodríguez, C., Rosa, D. & Olle, J. Artificial intelligence discovery of a charging protocol in a micromaser quantum battery. *Phys. Rev. A* **108**, 042618 (2023).
46. Santos, T. F. F., de Almeida, Y. V. & Santos, M. F. Vacuum-enhanced charging of a quantum battery. *Phys. Rev. A* **107**, 032203 (2023).
47. Downing, C. A. & Ukhtary, M. S. A quantum battery with quadratic driving. *Commun. Phys.* **6**, 322 (2023).
48. Gemme, G., Andolina, G. M., Pellegrino, F. M. D., Sassetti, M. & Ferraro, D. Off-resonant Dicke quantum battery: Charging by virtual photons. *Batteries* **9**, 197 (2023).
49. Shaghaghi, V., Singh, V., Carrega, M., Rosa, D. & Benenti, G. Lossy micromaser battery: Almost pure states in the Jaynes-Cummings regime. *Entropy* **25**, 430 (2023).
50. Dou, F.-Q. & Yang, F.-M. Superconducting transmon qubit-resonator quantum battery. *Phys. Rev. A* **107**, 023725 (2023).
51. Gumberidze, M., Kolář, M. & Filip, R. Measurement induced synthesis of coherent quantum batteries. *Sci. Rep.* **9**, 19628 (2019).
52. Kamin, F. H., Tabesh, F. T., Salimi, S. & Santos, A. C. Entanglement, coherence, and charging process of quantum batteries. *Phys. Rev. E* **102**, 052109 (2020).
53. Shi, H.-L., Ding, S., Wan, Q.-K., Wang, X.-H. & Yang, W.-L. Entanglement, coherence, and extractable work in quantum batteries. *Phys. Rev. Lett.* **129**, 130602 (2022).
54. Arjmandi, M. B., Shokri, A., Faizi, E. & Mohammadi, H. Performance of quantum batteries with correlated and uncorrelated chargers. *Phys. Rev. A* **106**, 062609 (2022).
55. Arjmandi, M. B., Mohammadi, H., Saguia, A., Sarandy, M. S. & Santos, A. C. Localization effects in disordered quantum batteries. *Phys. Rev. E* **108**, 064106 (2023).
56. Farina, D., Andolina, G. M., Mari, A., Polini, M. & Giovannetti, V. Charger-mediated energy transfer for quantum batteries: An open-system approach. *Phys. Rev. B* **99**, 035421 (2019).
57. Carrega, M., Crescente, A., Ferraro, D. & Sassetti, M. Dissipative dynamics of an open quantum battery. *New J. Phys.* **22**, 083085 (2020).
58. Kamin, F. H., Tabesh, F. T., Salimi, S., Kheirandish, F. & Santos, A. C. Non-Markovian effects on charging and self-discharging process of quantum batteries. *New J. Phys.* **22**, 083007 (2020).
59. Zakavati, S., Tabesh, F. T. & Salimi, S. Bounds on charging power of open quantum batteries. *Phys. Rev. E* **104**, 054117 (2021).
60. Xu, K., Zhu, H.-J., Zhang, G.-F. & Liu, W.-M. Enhancing the performance of an open quantum battery via reservoir engineering. *Phys. Rev. E* **104**, 064143 (2021).
61. Arjmandi, M. B., Mohammadi, H. & Santos, A. C. Enhancing self-discharging process with disordered quantum batteries. *Phys. Rev. E* **105**, 054115 (2022).
62. Song, M.-L., Li, L.-J., Song, X.-K., Ye, L. & Wang, D. reservoir-mediated entropic uncertainty in charging quantum batteries. *Phys. Rev. E* **106**, 054107 (2022).
63. Hadipour, M., Haseli, S., Dolatkhah, H. & Rashidi, M. Study the charging process of moving quantum batteries inside cavity. *Sci. Rep.* **13**, 10672 (2023).
64. Mojaveri, B., Bahrbeig, R. J., Fasihi, M. A. & Babanzadeh, S. Enhancing the direct charging performance of an open quantum battery by adjusting its velocity. *Sci. Rep.* **13**, 19827 (2023).
65. Xu, K., Zhu, H.-J., Zhu, H., Zhang, G.-F. & Liu, W.-M. Charging and self-discharging process of a quantum battery in composite reservoirs. *Front. Phys.* **18**, 31301 (2023).
66. Morrone, D., Rossi, M. A. C., Smirne, A. & Genoni, M. G. Charging a quantum battery in a non-Markovian reservoir: A collisional model approach. *Quantum Sci. Technol.* **8**, 035007 (2023).
67. Catalano, A. G., Giampaolo, S. M., Morsch, O., Giovannetti, V. & Franchini, F. *PRX Quantum* **5**, 030319 (2024).
68. Mojaveri, B., Bahrbeig, R. J. & Fasihi, M. A. arXiv preprint arXiv:2405.11356, (2024).
69. Wu, L. A. & Segal, D. Quantum effects in thermal conduction: Nonequilibrium quantum discord and entanglement. *Phys. Rev. A* **84**, 012319 (2011).
70. Lambert, N., Aguado, R. & Brandes, T. Nonequilibrium entanglement and noise in coupled qubits. *Phys. Rev. B* **75**, 045340 (2007).
71. Quiroga, L., Rodriguez, F. J., Ramirez, M. E. & Paris, R. Nonequilibrium thermal entanglement. *Phys. Rev. A* **75**, 032308 (2007).
72. Sinaysky, I., Petruccione, F. & Burgarth, D. Dynamics of nonequilibrium thermal entanglement. *Phys. Rev. A* **78**, 062301 (2008).
73. Eisler, V. & Zimborás, Z. Entanglement negativity in the harmonic chain out of equilibrium. *New J. Phys.* **16**, 123020 (2014).
74. Hsiang, J.-T. & Hu, B. L. Nonequilibrium steady state in open quantum systems: Influence action, stochastic equation, and power balance. *Ann. Phys.* **362**, 139 (2015).
75. Hsiang, J.-T. & Hu, B. L. Quantum entanglement at high temperatures: Boson systems in nonequilibrium steady state. *High Energy. Phys.* **11**, 90 (2015).
76. Tavakoli, A., Haack, G., Huber, M., Brunner, N. & Brask, J. B. Heralded generation of maximal entanglement in any dimension via incoherent coupling to thermal baths. *Quantum* **2**, 73 (2018).
77. Hu, L.-Z., Man, Z.-X. & Xia, Y.-J. Steady-state entanglement and thermalization of coupled qubits in two common heat baths. *Quantum Inf. Process.* **17**, 45 (2018).
78. Tacchino, F., Auffèves, A., Santos, M. F. & Gerace, D. Steady state entanglement beyond thermal limits. *Phys. Rev. Lett.* **120**, 063604 (2018).

79. Wang, Z., Wu, W. & Wang, J. Steady-state entanglement and coherence of two coupled qubits in equilibrium and nonequilibrium reservoirs. *Phys. Rev. A* **99**, 042320 (2019).
80. Johansson, J. R., Nation, P. D. & Nori, F. QuTiP: An open-source Python framework for the dynamics of open quantum systems. *Comp. Phys. Comm.* **183**, 1760–1772 (2012).
81. Liao, J.-Q., Huang, J.-F. & Kuang, L.-M. Quantum thermalization of two coupled two-level systems in eigenstate and bare-state representations. *Phys. Rev. A* **83**, 052110 (2011).

Acknowledgements

Maryam Hadipour and Soroush Haseli acknowledge the Iran National Science Foundation (INSF) for supporting this work under project No.4039863. This work is based upon research funded by Iran National Science Foundation (INSF) under project No.4039863

Author contributions

Maryam Hadipour and Soroush Haseli all contributed to the development and completion of the idea, performing the calculations, analyzing the results, discussions and writing the manuscript.

Declarations

Competing interests

The authors declare no competing interests.

Additional information

Correspondence and requests for materials should be addressed to S.H.

Reprints and permissions information is available at www.nature.com/reprints.

Publisher's note Springer Nature remains neutral with regard to jurisdictional claims in published maps and institutional affiliations.